Macromolecules

Cite This: Macromolecules 2018, 51, 8721−8728

Article

pubs.acs.org/Macromolecules

Interferometric Technique To Determine the Dynamics of Polymeric Fluids under Strong Confinement

Luisa G. Cencha,[†] Raul Urteaga,*[,†] and Claudio L. A. Berli[‡]

[†]IFIS-Litoral, Universidad Nacional del Litoral-CONICET, Güemes 3450, 3000 Santa Fe, Argentina

[‡]INTEC, Universidad Nacional del Litoral-CONICET, Predio CCT CONICET Santa Fe, RN 168, 3000 Santa Fe, Argentina

Supporting Information

ABSTRACT: This work presents a new technique to study polymers under strong geometrical confinement in nanoporous films. The procedure is based on sensing the changes of the optical properties of the porous matrix due to polymer imbibition into the pores by using optical interferometry. A simple theoretical model is used to correlate the time-dependent optical thickness of the film with the polymer dynamics as a function of temperature. To test the method applicability, the imbibition of ethyl vinyl acetate in porous silicon membranes was studied. A large variation of the polymer viscosity was measured by varying the temperature from 20 to 110 °C. In addition, the confinement degree was varied in about 2 orders of magnitude by using matrices with different pore radius. A remarkable decrease in the viscosity was observed when the mean pore radius was reduced. Moreover, the interferometric technique enables the study of very low molecular weight polymers as well as measuring along a wide range of temperatures in a single nondestructive experiment.

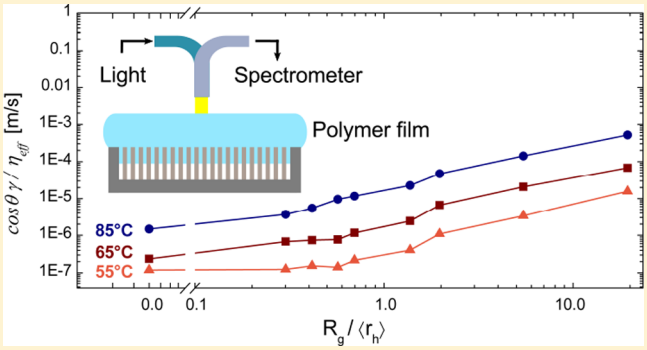

INTRODUCTION

The behavior of polymers in nanoscale confinement is currently of high interest in fundamental and applied sciences. Several works studying typical process and characteristics of polymers under strong geometrical constraints have been reported, including crystallization,[1−6] glass transition temperature,[7−9] mechanical properties,[8,10,11] polymer dynamics,[5,12,13] capillary flow,[2,5,14−20] and effective viscosity,[16,18,21−23] among others. The outcome of this research is also promising for applications in genetics and medicine. For example, the confinement of DNA molecules allows a linear unscrolling of the genome, which is desired for a simpler sequencing analysis.[24] In addition, it has been proven that a confined polymer model can help to understand the chromosome organization in elongated bacterial cells.[25] The infiltration of polymers in porous materials is also of interest for obtaining nanocomposites, where porous matrices are used as templates for molten polymers.[26−30] Concerning the fundamentals, it has been demonstrated that when forced to flow through nanometer scale pores, polymeric fluids exhibit properties different from those measured in bulk flow;[2] nowadays, the explanation of this fact is one of the major concerns in the field of soft matter. Furthermore, the existing methods to characterize bulk polymers are not always appropriate to study polymeric fluids in small confinements.[11]

In this context, the present work describes an interferometric technique to obtain rheological information about polymers under nanoconfinement. It involves the measurement and analysis of the imbibition dynamics of polymers in porous thin films. As a representative example, the imbibition of poly(ethylene vinyl acetate) (EVA) into mesoporous silicon films was studied. EVA is a well-known thermoplastic exhibiting the typical behavior of polymeric fluids. We had previously reported an optical technique based on laser interferometry with submillisecond resolution to investigate the dynamics of capillary-driven fluid imbibition in nanoporous substrates.[31−33] The technique has been further improved, and here the reflectance spectrum is used to instantaneously track the infiltration of a polymer into porous silicon films, while temperature is varied in a controlled fashion. A simple theoretical model is then used to correlate the evolution of the polymer front position to the effective polymer viscosity as a function of temperature.

The paper is organized as follows. The section "Theory" describes the procedure to extract the effective viscosity of the confined polymer from the infiltration dynamics data. The section "Methods and Materials" presents the porous silicon fabrication method, characteristics of the materials used, and the setup of the interferometric technique. The section "Results and Discussion" displays the experimental results together with discussions of the main findings. Finally, the main conclusions are summarized.

Received: July 16, 2018
Revised: October 2, 2018
Published: October 25, 2018

DOI: 10.1021/acs.macromol.8b01504
Macromolecules 2018, 51, 8721−8728

THEORY

Problem Statement. The proposed technique allows one to assess the dynamics of polymer imbibition into the porous structure; more precisely, the fluid front position as a function of time can be obtained by recording of the light reflectance variations during the imbibition process. The polymer fraction inside the porous structure increases during the imbibition; hence, the effective refractive index n_{eff} of the composite leads to a continuous shift of the reflectance peaks to larger wavelengths. The light reflectance variation stops when the refractive index (RI) reaches a constant value, i.e., when the porous layer is fully infiltrated with polymer. The product of n_{eff} by the film thickness is defined as the optical thickness e_{op}. At certain infiltration length x (see Figure 1b), the total optical thickness of the partially infiltrated membrane of thickness L can be calculated as the sum of partial contributions, i.e., $e_{op}(x) = n_{emp}(L - x) + n_{inf}x$, where n_{emp} and n_{inf} are the effective RI of the empty and infiltrated membrane, respectively. In particular, the normalized variation of the optical thickness, defined as $\Delta e_{op}(x) \equiv \frac{e_{op}(x) - e_{op}(0)}{e_{op}(L) - e_{op}(0)}$, provides the simple result $\Delta e_{op}(x) = \frac{x}{L}$.

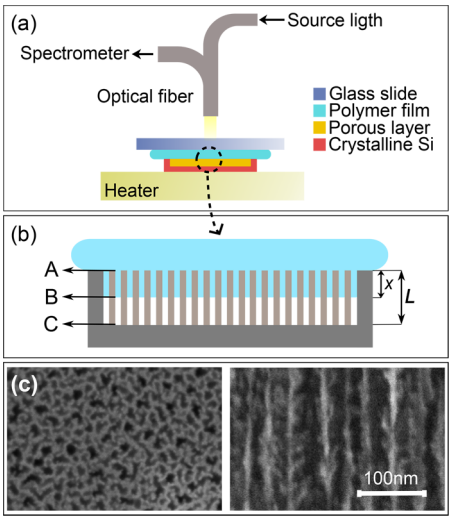

Figure 1. (a) Scheme of the experimental setup used for the interferometric measurements. The porous silicon membrane is placed onto the temperature-controlled plate with the polymer film on its upper surface. (b) Scheme of the polymeric fluid front position x in a porous silicon film of thickness L. A, B, and C are the three interfaces contributing to light reflection. (c) SEM images of top and side views of a porous silicon film with 20 nm pore mean hydraulic radius.

In this system, three interfaces contribute to the reflection of light (indicated as A, B, and C in Figure 1b). However, interface B, formed by the fluid front in the porous membrane, reflects a negligible intensity because the refractive index contrast is smaller than in the other two.[31,32] According to this, the reflectance will be dominated by the interference of the reflected beams at the porous membrane interfaces (A and C). In this case, the reflectance will show a maximum or a minimum when the phase shift between the reflected beams is a multiple of π, that is, when the optical thickness e_{op} is a multiple of $\lambda/4$ (a quarter of the wavelength of light).[31,32] This means that the wavelength at any particular extreme position in the reflectance spectrum (λ_e) is proportional to the membrane optical thickness at each time. Then, we can use the relative variation of λ_e to obtain the normalized fluid front position at each time, namely

$$\Delta\lambda_e(t) \equiv \frac{\lambda_e(t) - \lambda_e(0)}{\lambda_e(t_{fill}) - \lambda_e(0)} = \frac{x(t)}{L} \quad (1)$$

where $\lambda_e(0)$ and $\lambda_e(t_{fill})$ are the wavelength at a particular extreme position at the beginning and at the end of the imbibition process, respectively. In this way, tracking the position of the extremes in the reflectance spectrum can be used to measure the evolution of the fluid front position inside the porous membrane. In addition, noise reduction can be achieved by averaging the position of multiple extreme positions.

An alternative way to obtain the optical thickness evolution of the porous silicon layer during the imbibition process is by using reflectometric interference Fourier transform spectroscopy (RIFTS).[34] Here, the Fourier transform is computed from the reflectance data in the frequency domain, and the peak position obtained at each time corresponds to the instantaneous optical thickness of the porous silicon film. In this work we use both methods to measure the fluid front position, obtaining identical results in both cases.

Fluid Dynamic Model. The capillary filling of polymeric liquids in nanopore matrices is commonly described by using the Lucas–Washburn (LW) equation.[5,7,17−20,22,23] Here we use a modified version of that model[31]

$$x(t) = \sqrt{\frac{\gamma\langle r_h\rangle \cos\theta}{2\eta\tau^2}}\sqrt{t} \quad (2)$$

where the proportionality factor between the liquid front position x and the square root of time t includes physical parameters of the fluid (surface tension γ, contact angle θ, and viscosity η) and parameters related to the morphology of the porous structure (the tortuosity, τ, and the mean hydraulic radius, $\langle r_h\rangle$). The hydraulic radius is defined as $2A/P$, where A is the cross-sectional area and P is the perimeter of the pore, and the average is weighted by the cross-sectional area.[31] The tortuosity takes into account the orientation of the pores in the disordered structure and is defined as $\tau = x_{eff}/x$, where x_{eff} is the actual distance traveled by the fluid in the pore space and x is the straight distance measured along the flow direction. In addition, one may define the filling time $t_{fill} = t(x = L)$ as the time taken by the polymer to fully infiltrate the porous silicon membrane.

Combining eq 2 and eq 1 yields

$$\Delta\lambda_e = \beta\sqrt{t} \quad (3)$$

where β is defined as

$$\beta = \frac{1}{L}\sqrt{\frac{\gamma\langle r_h\rangle \cos\theta}{2\eta\tau^2}} \quad (4)$$

The time derivative of eq 3 is

$$\frac{d\Delta\lambda_e}{dt} = \frac{\beta}{2\sqrt{t}} \quad (5)$$

Considering that $\Delta\lambda_e = 1$ at the filling time (see eq 1), then $t_{fill} = 1/\beta^2$, and including β from eq 5, we obtain

$$t_{fill} = \frac{1}{2\frac{d\Delta\lambda_e}{dt}\Delta\lambda_e} = \frac{2L^2\tau^2}{\phi\langle r_h\rangle} \quad (6)$$

DOI: 10.1021/acs.macromol.8b01504
Macromolecules 2018, 51, 8721−8728

where $\phi = \gamma \cos\theta/\eta$ is a parameter involving fluid properties. Despite a factor 2, ϕ was defined by Washburn as the penetrativity of a given liquid,[35] which has velocity units.

The imbibition process was performed in two different ways: at constant temperature and with a linear increase of temperature. In the first case, the direct measurement of the filling time can be used to obtain ϕ at that temperature, provided the other parameters are known. When a linear increase of temperature is used, the instantaneous value of $\Delta\lambda_e$ (and its time derivative) can be used in eq 6 to obtain $\phi(T)$ at each temperature T. In this case, $t_{fill}(T)$ represents the time taken by the polymer to fill the porous layer in an assay made at the temperature T. In fact, measurements at constant temperature were used to experimentally validate eq 6, as discussed later. In this way, the properties of the fluid can be measured for a wide range of temperatures in a single experiment.

Calibration of the Porous Silicon Structure. To obtain $\phi(T)$ from the eq 6, it is necessary to measure the factor related to the membrane morphology $(2L^2\tau^2/\langle r_h\rangle)$. This structural term can be independently quantified by using a calibration fluid, i.e., a fluid of known parameter ϕ_{cf}, at a given temperature. The chosen calibration fluid was glycerol (>99.5%), mainly due to its relatively high viscosity, which is desired to measure large enough filling times. Once the filling time of the calibration fluid t_{fill}^{cf} is known, the polymer parameter, ϕ_{pol}, can be obtained as follows

$$\phi_{pol} = \phi_{cf}\frac{L_{pol}^{\ 2}}{L_{cf}^{\ 2}}\frac{t_{fill}^{cf}}{t_{fill}^{pol}} \tag{7}$$

where t_{fill}^{pol} is the corresponding filling time for the polymer imbibition. The calibration measurements were performed at 20 °C in porous silicon films of thickness $L_{cf} = 15\mu$m (3 times larger than membrane thickness used in EVA measurements, L_{pol}). This allowed a more accurate determination of t_{fill}^{cf} due to the very fast imbibition of glycerol in thin porous silicon membranes.

METHODS AND MATERIALS

Porous Silicon Membranes. The mesoporous silicon membranes were made by electrochemical anodization of crystalline silicon, p-type, boron dopant, orientation [100], and resistivity 1−5 mΩ·cm, provided by Topsil Semiconductor Materials SA, USA. The silicon acts as the anode of an electrochemical cell, where the electrolyte is a solution of fluorhydric acid and ethanol (1 HF(50%):2 EtOH). The porosity and mean pore size of the membranes are defined by the current density used during anodization, whereas the anodization time defines the thickness of the films. Ten different values of current densities were used, ranging from 12 to 118 mA/cm^2, which gave porosities between 50% and 90% and mean radius between 1 and 70 nm approximately. For more details of the membrane characterization see the Supporting Information (Figure S2).

Thermoplastic Polymer Films. The polymer used to infiltrate the pores was ethyl vinyl acetate copolymer (EVA) with 28 wt % vinyl acetate comonomer content, Elvax 260 from Dupont. The polymer density at 23 °C is $\rho = 955$ kg/m^3, and the melt flow rate (190 °C/2.16 kg) is 6 g/10 min. The molecular weight distribution of the EVA samples was done by gel permeation chromatography (GPC) using a Viscotek 3500A HT instrument with refractive index, viscosity, and ligth scattering detectors. The polymer was dissolved in trichlorobenzene, and measurement was performed at 145 °C. The samples were eluted through two PLGel Mixed-A 20 μm columns (Polymer Laboratories). Calibration was done using polystyrene. Results indicate that the commercial polymer tested has a broad monomodal molecular weight distribution (as shown in Figure S10 of the Supporting Information). The following distribution parameters were obtained: number-average molecular weight, M_n = 19000 g/mol, weight-average molecular weight M_w = 118000 g/mol, peak position molecular weight M_p = 41000 g/mol, polydispersity index $D = M_w/M_n$ = 6.2, and radius of gyration R_g = 22.13 nm.

A dynamic mechanical thermal analysis (DMTA) was used to determine the complex bulk viscosity of the polymer as a function of temperature. Measurements were performed at 10 rad/s (1.6 Hz) under cooling and heating conditions on a shear rheometer (ARES) with 6 mm parallel plates and a gap thickness of 1.173 mm. The strain was varied between 2% and 0.01%, and the heating/cooling rate was 2 K/min. The measured curves of the storage and loss modulus (G' and G'', respectively) as well as the calculated complex viscosity can be found in the Supporting Information (Figure S3). The complex viscosity was calculated by the empirical Cox−Merz "rule",[36] $\eta^* = \sqrt{(G'/\omega)^2 + (G''/\omega)^2}$, which has been successfully employed in many polymeric systems to describe the correspondence between the steady shear viscosity as a function of shear rate and the magnitude of the complex viscosity as a function of the angular frequency. The complex bulk viscosity was also measured at a second frequency (10 Hz) to analyze possible differences in the rehology of the polymer due to its shear thinning behavior. A comparison between the results at both frequencies is shown in Figure S4. As the curves practically overlap, one can conclude that the polymer viscosity is independent of the shear rate at these (and hence at lower) frequencies.

The molecular weigth between entanglements (M_e = 470 g/mol) was determined from the relation $G' = \rho RT/M_e$,[37] where R is the ideal gas constant and T = 23 °C.

Polymer films were obtained by pressing a solid pellet (~2 g) between two glass slides and heating at 90 °C in an oven for 2 min; thus, a film of ~100 μm thickness was obtained. After cooling at room temperature, one of the glass slides was separated to allow the polymer films to come into contact with the porous silicon surface (see Figure 1a).

The initial crystallinity X_c^0 of the films is around 4.5% and it was determined from DSC measurements on a TA Instruments differential scanning calorimeter (Q2000). It was calculated from the enthalpy of fusion of the film (ΔH_f = 12.5 J/g) and the enthalpy of fusion of the perfect polyethylene crystal (ΔH_f^* = 277.1 J/g)[38] as $X_c^0 = (\Delta H_f/\Delta H_f^*) \times 100\%$. This measurement can be found in Figure S5.

Interferometric Technique. The experimental setup consists of a UV−vis−NIR spectrometer (Ocean Optics HR4000) with an R400-7-SR fiber-optic reflection probe and a temperature-controlled plate. The porous silicon membrane is placed over the heater, and when a thin layer of polymer is deposited on its surface, the measurement of the reflectance spectra begins at regular intervals. A scheme of the arrangement is presented in Figure 1a. The polymer film is placed onto the porous silicon surface, and a slight pressure is made over the attached glass slide. The optical fiber guides the light from the lamp to the porous silicon membrane and collect the reflected light, taking it back to the spectrometer. When the polymer begins to infiltrate into the pores by capillary action, the reflectance peaks move to the right as a consequence of the increase in n_{eff}. An example of this process is shown in Figure S1b.

RESULTS AND DISCUSSION

Membranes Morphology Caracterization. The porosity and optical thickness of the porous silicon membranes (fabricated with different anodization current densities) were estimated by fitting its reflectance spectra using the Looyenga−Landau−Lifshitz (LLL) mixing rules[39,40] for effective mediums. An almost linear relation between the current density and porosity was obtained. A typical LLL fit and the obtained current density−porosity curve can be found in Figures S1a

DOI: 10.1021/acs.macromol.8b01504
Macromolecules 2018, 51, 8721−8728

and S2, respectively. Typical imbibition measurements of membrane calibration are shown in Figure 2a. This figure

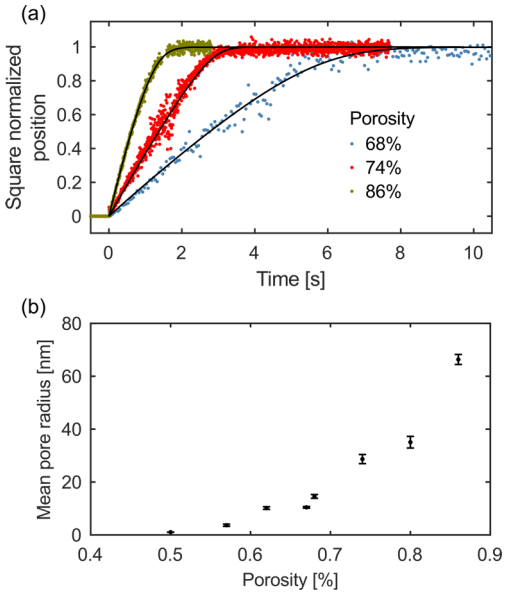

Figure 2. (a) Square normalized position as a function of time for the imbibition of glycerol in 15 μm thickness porous silicon films with different porosities. Symbol are experimental data, and lines are the fitting curves (see text for details). (b) Mean pore hydraulic radius $\langle r_h \rangle$ of porous silicon membranes as a function of the porosity obtained from eq 6 by using t_{fill} data of glycerol from the fitting curves in (a).

shows the filling dynamics of glycerol in porous silicon layers of different porosities and 15 μm thickness. The symbols are the experimental data, and the continuous lines are the fitting curves with a model equation that takes into account the air trapped in the pores.[31] In the case of glycerol, the final fraction of filled pores varies from 95% for the larger pores to 99% for the smaller ones. This fraction is one of the free parameters used in the fitting model showed in the Figure 2a. The obtained values are in reasonable accordance to those expected using the mean radius of the pores.[31] See Figure S6 for the results of glycerol imbibition in porous silicon membranes of other porosities.

The good agreement between model and experiments leads to conclude that the dynamics is consistent with a uniform porous matrix, considering an hydraulic mean radius representative of the porous structure; therefore, the deviations from $x \propto \sqrt{t}$ should emerge from the non-Newtonian behavior of the polymeric fluids. As expected for a simple Newtonian fluid like glycerol, the filling time decreases as the mean hydraulic radius increases.

The mean hydraulic pore radius for each porosity was obtained from eq 6 as $\langle r_h \rangle = 2\phi_{cf}\tau^2/t_{fill}$, where t_{fill} was experimentally obtained from Figure 2a, whereas the values of $\phi_{cf} = 0.037$ m/s[41−43] and $\tau \simeq 2.6$[31] were taken from the literature. Results are presented in Figure 2b, where it can be seen that $\langle r_h \rangle$ increases with porosity.

Polymer Imbibition. *Temperature-Dependent Dynamics.* The reflectance spectra of the PS membranes were recorded at regular time intervals during the imbibition of EVA, and then the temporal evolution of a peak position was used to calculate the normalized position of the fluid front (eq 1). Figure 3a shows the results obtained in porous silicon films

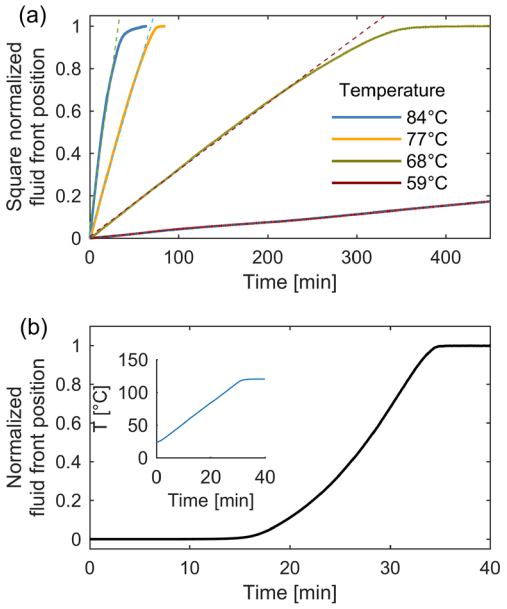

Figure 3. Imbibition dynamics of EVA in porous silicon films of $\langle r_h \rangle$ = 66 nm and 5 μm thickness. (a) Square normalized fluid front position as a function of time for different fixed temperatures and linear fit in the first 80% of the filling fraction for all measured temperatures (mean $R^2 = 0.995$). (b) Normalized fluid front position as a function of temperature obtained by applying a heating ramp of 2 °C/min (inset).

of 5 μm and 86% porosity ($\langle r_h \rangle$ = 66 nm) at different constant temperatures. The imbibition rate increases with temperature due to the corresponding reduction of polymer viscosity.

An estimation of the shear rate ($\dot{\gamma}$) at the inner wall of the pores is given by $\dot{\gamma} = 4\langle v \rangle / r$, where $\langle v \rangle$ is the mean velocity of the fluid front.[44] As predicted by Lucas−Washburn dynamics, the capillary imbibition exhibits a velocity proportional to the pore radius, $\langle v \rangle = 2r\gamma \cos\theta/\eta x$. Therefore, in capillary driven flows, the shear rate becomes independent of the pore radius. This fact is also valid for non-Newtonian fluids, as demonstrated in a previous paper.[45] An estimation of $\dot{\gamma}$ is included in Figure S9 for the situation of Figure 3b. It was found that $\dot{\gamma} < 0.1\ s^{-1}$ during the entire process. Because of any dependence of $\dot{\gamma}$ with the pore radius is expected, this value is representative of all the experiments performed in this work. Because of this, the $\dot{\gamma}$ value is well below the frequencies in which the complex viscosity of bulk EVA was tested (Figure S4) and does not show evidence of other than Newtonian behavior; it is concluded that the shear rate developed during capillary imbibition into the pores corresponds also to the range of Newtonian behavior. In other words, the shear-thinning behavior of the bulk polymer is evident at higher shear rates only and should not play a role in the effective viscosity η_{eff} measured in our system.

On the other hand, in this case it is not expected that the air compression at the pores ends be relevant given the long time available to be evacuated. The small curvature at the end of the filling process is associated with the front widening effect due to pore size dispersion in the membrane.[2]

As mentioned before, also measurements with a linear increase of temperature were performed. Figure 3b shows a typical curve measured with a heating ramp of 2 °C/min (inset). It is worth noting that since the crystalline silicon substrate is relatively thin (500 μm) and its thermal diffusivity

DOI: 10.1021/acs.macromol.8b01504
Macromolecules 2018, 51, 8721−8728

is rather high (0.8 cm^2/s), one may certainly assume that the temperature at the porous silicon film is that set at the heating plate.

As it was previously defined, t_{fill} corresponds to the time at which the optical thickness reaches its maximum value. Using the experimental values of t_{fill} (obtained from Figure 3a) and knowing the calibration parameters, ϕ_{EVA} was calculated for each temperature from eq 7. Besides, assuming that the Lucas–Washburn dynamics is (intantaneously) satisfied at each time during the imbibition, ϕ_{EVA} as a function of temperature was also obtained from eq 6 by using the continuous curve reported in Figure 3b. Both results are compared in Figure 4, where a remarkable agreement is observed. This result demonstrates the accuracy of assuming Lucas–Washburn dynamics for the imbibition with a linear increase of temperature.

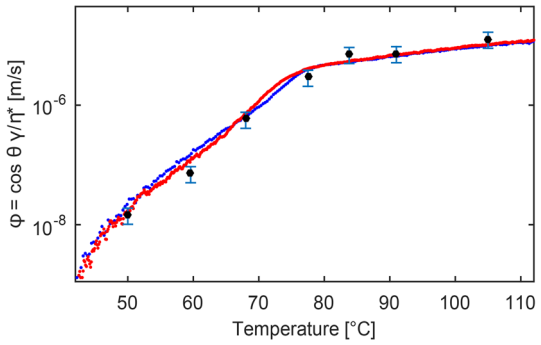

Figure 4. Parameter ϕ_{EVA} as a function of temperature in a porous silicon membrane of 86% porosity. Black barred circles correspond to measured values at constant temperature (Figure 3a) while red and blue points were obtained by using a temperature ramp of 2 °C/min (Figure 3b).

In Figure 4, a marked increase of ϕ_{EVA} with temperature is observed. Because the surface tension is not expected to change appreciably[46] and the measured contact angle θ is almost constant (see Figure S7), this behavior can be interpreted as a strong decrease of the effective viscosity with temperature. The linear behavior in this semilog plot is typical of thermally activated, Arrhenius-like processes.[47]

Effective Viscosity under Confinement. To analyze the effect of confinement on the polymer rheology, measurements of ϕ_{EVA} as a function of temperature were performed in porous silicon films with different mean pore radii. Typical curves presented in Figure 5 shows that ϕ_{EVA} decreases more than 2 orders of magnitude when $\langle r_h \rangle$ increases from about 1 to 66 nm. These results are in agreement with previous reports on similar systems, where a decrease of the effective viscosity is measured in strong confined polymers.[14,16,18] In addition, to make a comparison with the properties of the polymer in bulk conditions, the value of ϕ_{EVA}^{bulk} was calculated using the measured complex viscosity and contact angle (see Figures S4 and S7) and surface tension value obtained from the literature.[46]

Because it is known that pressure can impact the dynamics of EVA due to the increase in the crystalline component,[48] we estimate the capillary pressure in the membranes, which is maximum in the smallests pores. Taking into account our values of X_c^0 and pressure, it may inferred that the potential pressure-induced increase in crystallinity has a negligible impact on the dynamics of imbibition reported here.

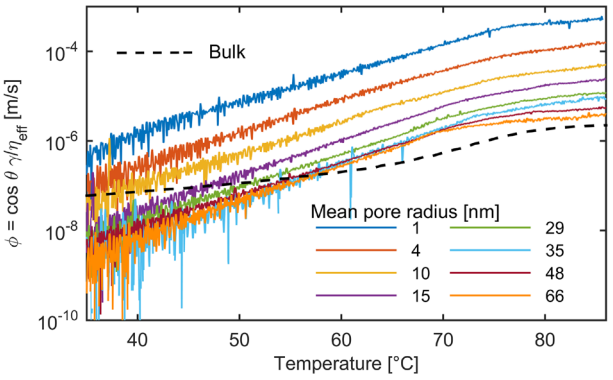

Figure 5. Parameter ϕ_{EVA} as a function of temperature for different mean pore radii. The polymer parameter ϕ_{EVA}^{bulk} in bulk conditions is also included as a dashed line.

It is known that certain properties of polymers under confinement can be affected by the oligomers content in the sample.[49] In this work a commercial polymer having a broad monomodal molecular weight distribution is studied (polydispersity index 6.2). However, we assumed that in the analysis of the parameter ϕ_{EVA} this fact is not relevant when comparing the results with the theoretical bulk parameter value (ϕ_{EVA}^{bulk}). Zhang et al. have shown that polymer chains having different sizes in the melt state (without solvent) can be fractionated via the imbibition in nanopores[50] and attribute this fact to the presence of two different wetting mechanisms: complete and partial wetting. The prevalence of one or another is given by the wetting transition temperature (T_w), at which the contact angle of the polymer is zero, $\theta(T_w) = 0°$. Partial wetting occurs when $T < T_w$ is satisfied; this situation corresponds to the classical capillary imbibition with the presence of a polymeric meniscus. On the other hand, complete wetting occurs when $T > T_w$. In this case a polymeric precursor film is formed in the pore walls. The latter process is considerably faster than the classical capillary imbibition.[50] As the wetting temperature is a function of the polymer molecular weight, $T_w(M_w)$, it is possible that for a given temperature a polymer melt containing chains of several sizes be fractionated, where the smaller molecules are fractionated first. This fact has been reported for bimodal molecular weight distributions in alumina nanopores.[19,50] In this work, the parameter ϕ_{EVA} is analyzed in a temperature range in which $\theta \sim 51°$. Additionally, as previously mentioned, it is not expected a considerably variation of this value in the tested temperatures. Because the EVA contact angle is relatively large, it can be certainly assumed the prevalence of the partial wetting regime in the presented experiments, and hence a fractioning of the polymer is not expected.

To better visualize the confinement effect, ϕ_{EVA} was plotted as a function of the confinement degree $R_g/\langle r_h \rangle$ at different temperatures in Figure 6a. Here $R_g \approx 22$ nm is the radius of gyration of the polymer. Despite an apparent minimum around $R_g/\langle r_h \rangle = 0.5$ for the lower temperatures, all the ϕ_{EVA} curves in Figure 6a shows a similar behavior: the filling velocity increases with the confinement. It is worth to highlight that in the results shown in Figures 5 and 6, no assumption has been made about the effect of confinement in surface tension and contact angle. If these parameters change with respect their bulk values, as the viscosity does, then this effect is already comprised in the reported values of ϕ_{EVA}.

DOI: 10.1021/acs.macromol.8b01504
Macromolecules 2018, 51, 8721–8728

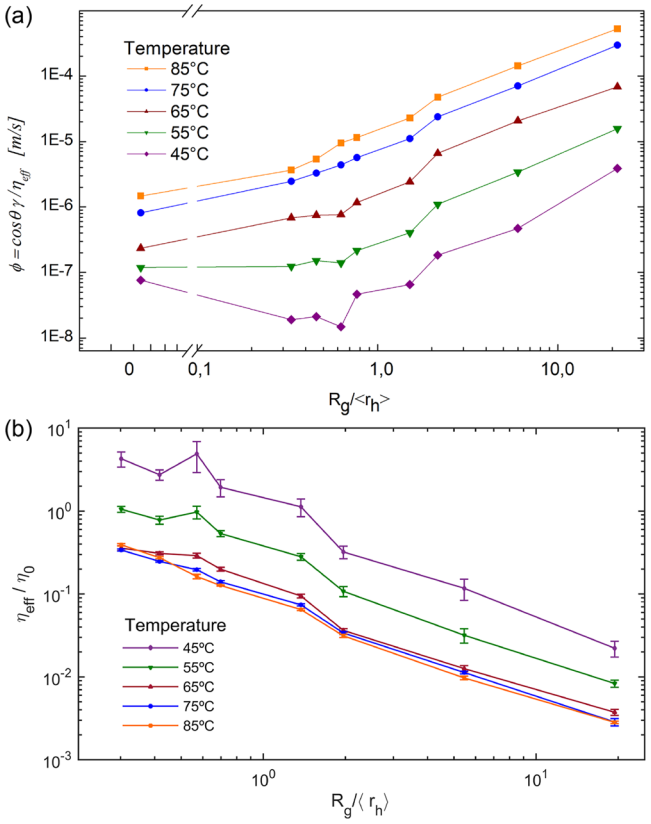

Figure 6. (a) Parameter ϕ_{EVA} as a function of the confinement degree $R_g/\langle r_h\rangle$ for different temperatures. (b) Ratio of the effective to bulk viscosity η_{eff}/η_0 as a function of $R_g/\langle r_h\rangle$ for different temperatures, assuming that the surface tension and the contact angle do not change considerably in the confined state.

Provided that the values of γ and θ under strong confinement are similar to those in the bulk, as it is usually assumed in the literature,[17,18,22,23] one may write $\phi_{bulk}/\phi_{EVA} = \eta_{eff}/\eta_0$, where η_0 is the bulk complex viscosity. This ratio as a function of $R_g/\langle r_h\rangle$ is shown in Figure 6b.

The effect of considering the static contact angle (θ_e) instead the dynamic contact angle (θ_d), which depends on the velocity of the three-phase contact line, was analyzed by Yao et al.[18] and Cao et al.[17] in their works about the imbibition of poly(ethylene oxide) and polyethylene melts in nanoporous alumina, respectively. Both authors reported that the differences found between the imbibition dynamics in the confined state and the predicted LW dynamics for the bulk are considerably larger than the differences expected from the consideration of one or another contact angle (θ_e or θ_d). On the other hand, Hor et al.[22] reported that the effective viscosity of poly(styrene) and poly(2-vinylpyridine) confined in a dense packing of silica nanoparticles is robust across a range of estimated θ and $\gamma(T)$ parameters. To corroborate this assumption, a sensitivity test of ϕ_{bulk} with respect to the contact angle and the surface tension values was performed by testing two additional extremes contact angles (45° and 55°) besides the reported mean value and considering other fitting relations in calculating the polymer surface tension.[46] This analysis is presented in Figure S8.

The results showing a strong decrease in the effective viscosity with the increase in the confinement degree can be explained by a mechanism based on the reptation model, proposed by Johner et al.[15] In this context, material transport is driven by a pressure gradient across a network of constraints (entanglements), mainly due by the reptation of free polymer chains. On the other hand, Yao et al. developed a unified theory to account for their experimental results about the opposite trends exhibited by the effective viscosity of poly(ethylene oxide) melts as a function of the molecular weight.[18−20] They have shown, by theory and experiments, that the reptation mechanism becomes dominant at a certain degree of confinement ($R_g \gg r$) and that the effective viscosity follows the relation $\eta_{eff} \propto N$, instead the common relation $\eta \propto N^3$ for bulk polymer viscosity (N being the number of monomers in a polymeric chain). In other words, the reptation of polymer chains under strong confinement enhances the mobility of confined chains, leading to faster imbibition process.[15,20] Our experimental results agree with this mechanism, where the decrease in effective viscosity becomes more noticeable when $R_g/\langle r_h\rangle > 1$, for all the tested temperatures.

Thermal Transitions under Confinement. In Figure 5, a change of the slope is observed around the bulk EVA melting point (75 °C; see Figure S5). Even though the tendency of this characteristic temperature with the confinement is not well-defined, the results suggests that the interferometric technique could be also useful to characterize phase transitions in polymers. Other authors had reported a decrease in the melting point due to the confinement effects.[6,51] This fact may be related to the decrease in the degree of crystallinity when the polymer is geometrically confined.[52,53]

CONCLUSIONS

The technique presented in this work enables the determination of the capillary filling dynamics of a polymeric fluid in a porous structure by means of interferometric measurements. Because of the high spatial resolution inherent to the technique, measurements range from relatively high imbibition velocities, limited only by the acquisition time of the spectra (a few milliseconds), to very slow speeds, limited only by the duration of the experiment (hours). This allows one to measure the capillary filling of simple liquids such as glycerol as well as polymeric liquids with viscosities 5 orders of magnitude higher. In addition, this range can be further extended by using membranes of different thickness, depending on the effective viscosity of the fluid. It is worth noting that other than porous silicon structures can be employed, expanding the application area to the analysis of several pore geometries and polymer−substrate interactions. On the other hand, measuring the relative position of the fluid front (and its time derivative) enables instant measurement of fluid properties. In addition, a continuous variation of the temperature permit to explore the behavior of the fluid over a wide range of temperatures in a single experiment. This advantage of the technique also permits to determine the effect of confinement on phase transitions such as the polymer melting point in a wide range of viscosities and hence over polymers with very different molecular weights.

ASSOCIATED CONTENT

Supporting Information

The Supporting Information is available free of charge on the ACS Publications website at DOI: 10.1021/acs.macromol.8b01504.

DOI: 10.1021/acs.macromol.8b01504
Macromolecules 2018, 51, 8721−8728

Figure S1: evolution of the porous silicon reflectance during imbibition and LLL fit; Figure S2: porous silicon porosity as a function of the anodization current density; Figure S3: DMTA measurements of EVA; Figure S4: DMTA measurements of EVA at different frequencies; Figure S5: DSC measurements of EVA; Figure S6: glycerol imbibition results in porous silicon membranes of several porosities; Figure S7: contact angle measurement of EVA in crystalline silicon; Figure S8: sensitivity analysis; Figure S9: shear rate during the imbibition of EVA; Figure S10: GPC EVA molecular weight distribution (PDF)

AUTHOR INFORMATION

Corresponding Author

*E-mail urteagar@santafe-conicet.gov.ar; Ph +54 342 4559174; Fax +54 342 4550944.

ORCID

Luisa G. Cencha: 0000-0003-2858-6827

Claudio L. A. Berli: 0000-0002-1321-6738

Notes

The authors declare no competing financial interest.

ACKNOWLEDGMENTS

The current work was supported by the CONICET, ANPCyT (Grant PICT-2015-1051), and the Universidad Nacional del Litoral (Grants CAI+D-78-50120110100010-0 and 50420150100108LI), Argentina. DMTA measurements by Dr. Kaloian Koynov (MPI-P, Mainz, Germany) and the collaboration of Dr. Ignacio Helbling (INTEC, Santa Fe, Argentina) are gratefully acknowledged.

REFERENCES

(1) Michell, R. M.; Lorenzo, A. T.; Müller, A. J.; Lin, M.-C.; Chen, H.-L.; Blaszczyk-Lezak, I.; Martín, J.; Mijangos, C. The Crystallization of Confined Polymers and Block Copolymers Infiltrated Within Alumina Nanotube Templates. *Macromolecules* **2012**, *45*, 1517−1528.

(2) Huber, P. Soft matter in hard confinement: phase transition thermodynamics, structure, texture, diffusion and flow in nanoporous media. *J. Phys.: Condens. Matter* **2015**, *27*, 103102.

(3) Houachtia, A.; Alcouffe, P.; Boiteux, G.; Seytre, G.; Gerard, J.-F.; Serghei, A. Nanofluidics Approach to Separate between Static and Kinetic Nanoconfinement Effects on the Crystallization of Polymers. *Nano Lett.* **2015**, *15*, 4311−4316.

(4) Shingne, N.; Geuss, M.; Thurn-Albrecht, T.; Schmidt, H.-W.; Mijangos, C.; Steinhart, M.; Martín, J. Manipulating Semicrystalline Polymers in Confinement. *J. Phys. Chem. B* **2017**, *121*, 7723−7728.

(5) Yao, Y.; Suzuki, Y.; Seiwert, J.; Steinhart, M.; Frey, H.; Butt, H.; Floudas, G. Capillary Imbibition, Crystallization, and Local Dynamics of Hyperbranched Poly(ethylene oxide) Confined to Nanoporous Alumina. *Macromolecules* **2017**, *50*, 8755−8764.

(6) Yao, Y.; Sakai, T.; Steinhart, M.; Butt, H.-J.; Floudas, G. Effect of Poly(ethylene oxide) Architecture on the Bulk and Confined Crystallization within Nanoporous Alumina. *Macromolecules* **2016**, *49*, 5945−5954.

(7) Alexandris, S.; Papadopoulos, P.; Sakellariou, G.; Steinhart, M.; Butt, H.-J.; Floudas, G. Interfacial Energy and Glass Temperature of Polymers Confined to Nanoporous Alumina. *Macromolecules* **2016**, *49*, 7400−7414.

(8) Romo-Uribe, A. Polymers in 2D confinement: A nanoscale mechanism for thermo mechanical reinforcement. *Polym. Adv. Technol.* **2018**, *29*, 507−516.

(9) Hor, H. W. J. L.; Zhang, Y.; Liu, T.; Lee, D.; Fakhraai, Z. Dramatic Increase in Polymer Glass Transition Temperature under Extreme Nanoconfinement in Weakly Interacting Nanoparticle Films. *ACS Nano* **2018**, *12*, 5580−5587.

(10) Mijangos, C.; Hernández, R.; Martín, J. A review on the progress of polymer nanostructures with modulated morphologies and properties, using nanoporous AAO templates. *Prog. Polym. Sci.* **2016**, *54*−*55*, 148−182.

(11) Vogt, B. D. Mechanical and Viscoelastic Properties of Confined Amorphous Polymers. *J. Polym. Sci., Part B: Polym. Phys.* **2018**, *56*, 9−30.

(12) Dai, L.; Doyle, P. S. Comparisons of a Polymer in Confinement versus Applied Force. *Macromolecules* **2013**, *46* (15), 6336−6344.

(13) Martín, J.; Krutyeva, M.; Monkenbusch, M.; Arbe, A.; Allgaier, J.; Radulescu, A.; Falus, P.; Maiz, J.; Mijangos, C.; Colmenero, J.; Richter, D. Direct Observation of Confined Single Chain Dynamics by Neutron Scattering. *Phys. Rev. Lett.* **2010**, *104*, 104.

(14) Shin, K.; Obukhov, S.; Chen, J.-T.; Huh, J.; Hwang, Y.; Mok, S.; Dobriyal, P.; Thiyagarajan, P.; Russell, T. P. Enhanced mobility of confined polymers. *Nat. Mater.* **2007**, *6*, 961.

(15) Johner, A.; Shin, K.; Obukhov, S. Nanofluidity of a polymer melt: Breakdown of Poiseuille's flow model. *EPL* **2010**, *91*, 38002.

(16) Cuenca, A.; Bodiguel, H. Submicron flow of polymer solutions: slippage reduction due to confinement. *Phys. Rev. Lett.* **2013**, *110*, 108304.

(17) Cao, B.-Y.; Yang, M.; Hu, G.-J. Capillary filling dynamics of polymer melts in nanopores: experiments and rheological modelling. *RSC Adv.* **2016**, *6*, 7553.

(18) Yao, Y.; Alexandris, S.; Henrich, F.; Auernhammer, G.; Steinhart, M.; Butt, H.-J.; Floudas, G. Complex dynamics of capillary imbibition of poly(ethylene oxide) melts in nanoporous alumina. *J. Chem. Phys.* **2017**, *146*, 203320.

(19) Yao, Y.; Butt, H.; Zhou, J.; Doi, M.; Floudas, G. Capillary Imbibition of Polymer Mixtures in Nanopores. *Macromolecules* **2018**, *51*, 3059−3065.

(20) Yao, Y.; Butt, H.-J.; Floudas, G.; Zhou, J.; Doi, M. Theory on Capillary Filling of Polymer Melts in Nanopores. *Macromol. Rapid Commun.* **2018**, *39*, 1800087.

(21) Chen, F.; Peng, D.; Ogata, Y.; Tanaka, K.; Yang, Z.; Fujii, Y.; Yamada, N. L.; Lam, C.-H.; Tsui, O. K. C. Confinement Effect on the Effective Viscosity of Plasticized Polymer Films. *Macromolecules* **2015**, *48* (20), 7719−7726.

(22) Hor, J. L.; Wang, H.; Fakhraai, Z.; Lee, D. Effects of polymer-nanoparticle interactions on the viscosity of unentangled polymers under extreme nanoconfinement during capillary rise infiltration. *Soft Matter* **2018**, *14*, 2438−2446.

(23) Hor, J. L.; Wang, H.; Fakhraai, Z.; Lee, D. Effect of Physical Nanoconfinement on the Viscosity of Unentangled Polymers during Capillary Rise Infiltration. *Macromolecules* **2018**, *51*, 5069.

(24) Reisner, W.; Pedersen, J. N.; Austin, R. H. DNA confinement in nanochannels: physics and biological applications. *Rep. Prog. Phys.* **2012**, *75*, 106601.

(25) Ha, B.-Y.; Jung, Y. Polymers under confinement: single polymers, how they interact, and as model chromosomes. *Soft Matter* **2015**, *11*, 2333−2352.

(26) Li, Y. Y.; Cunin, F.; Link, J. R.; Gao, T.; Betts, R. E.; Reiver, S. H.; Chin, V.; Bhatia, S. N.; Sailor, M. J. Polymer Replicas of Photonic Porous Silicon for Sensing and Drug Delivery Applications. *Science* **2003**, *299*, 2045.

(27) Fedotov, A. Y.; Bakunova, N. V.; Komlev, V. S.; Barinov, S. M. Increase in Mechanical Properties of Porous Materials by Polymer Impregnation. *Inorganic Materials Applied Research* **2013**, *4*, 7−11.

(28) Wang, K.; Weissmüller, J. Composites of Nanoporous Gold and Polymer. *Adv. Mater.* **2013**, *25*, 1280−1284.

(29) Wang, J.; Lee, G. Y.; Kennard, R.; Barillaro, G.; Bisiewicz, R. H.; Lemus, N. A. C.; Cao, X. C.; Anglin, E. J.; Park, J. S.; Potocny, A.; Bernhard, D.; Li, J.; Sailor, M. J. Engineering the Properties of Polymer Photonic Crystals with Mesoporous Silicon Templates. *Chem. Mater.* **2017**, *29*, 1263−1272.

(30) Cheylan, S.; Sychevb, F.; Murzinab, T.; Trifonovc, T.; Maydykovskiyb, A.; Puigdollersc, J.; Alcubillac, R.; Badenesa, G.

DOI: 10.1021/acs.macromol.8b01504
Macromolecules 2018, 51, 8721−8728

Optical study of polymer infiltration into porous Si based structures. *Proc. SPIE* **2007**, *6593*, 65931K-1.
(31) Acquaroli, L.; Urteaga, R.; Berli, C.; Koropecki, R. Capillary Filling in Nanostructured Porous Silicon. *Langmuir* **2011**, *27*, 2067−2072.
(32) Urteaga, R.; Acquaroli, L. N.; Koropecki, R. R.; Santos, A.; Alba, M.; Pallarès, J.; Marsal, L. F.; Berli, C. L. A. Optofluidic Characterization of Nanoporous Membranes. *Langmuir* **2013**, *29*, 2784−2789.
(33) Urteaga, R.; Berli, C. L. In *Nanoporous Alumina: Fabrication, Structure, Properties and Applications*; Losic, D., Santos, A., Eds.; Springer Series in Materials Science; Springer International Publishing: 2015; Chapter 8, pp 249−268.
(34) Sailor, M. *Porous Silicon in Practice: Preparation, Characterization and Applications*; Wiley-VCH Verlag: 2012.
(35) Washburn, E. W. The Dynamics of Capillary Flow. *Phys. Rev.* **1921**, *17*, 273−283.
(36) Bird, R.; Curtiss, C.; Armstrong, R.; Hassager, O. *Dynamics of Polymeric Liquids*, 2 Vol. Set; Wiley: 1991.
(37) Unidad, H. J.; Goad, M. A.; Bras, A. R.; Zamponi, M.; Faust, R.; Allgaier, J.; Pyckhout-Hintzen, W.; Wischnewski, A.; Richter, D.; Fetters, L. J. Consequences of Increasing Packing Length on the Dynamics of Polymer Melts. *Macromolecules* **2015**, *48*, 6638−6645.
(38) Grulke, E. A.; Brandrup, J.; Immergut, E. H. In *Polymer Handbook*, 4th ed.; Abe, A., Bloch, D. R., Associate Eds.; Wiley-Interscience: Hoboken, NJ, 1999.
(39) Theiß, W. Optical properties of porous silicon. *Surf. Sci. Rep.* **1997**, *29*, 91.
(40) Landau, L.; Lifshitz, E. *Electrodynamics of Continuous Media*; Pergamon Press: 1984; Vol. *8*.
(41) Moldovan, A.; Bota, M.; Dorobantu, D.; Boerasu, I.; Bojin, D.; Buzatu, D.; Enachescu, M. Wetting properties of glycerol on silicon, native SiO_2, and bulk SiO_2 by scanning polarization force microscopy. *J. Adhes. Sci. Technol.* **2014**, *28*, 1277−1287.
(42) Haynes, W. *CRC Handbook of Chemistry and Physics*, 93rd ed.; 100 Key Points; Taylor & Francis: 2012.
(43) *Physical Properties of Glycerine and Its Solutions*; Glycerine Producers' Association: 1963.
(44) Darby, R. *Chemical Engineering Fluid Mechanics, Revised and Expanded*; Taylor & Francis: 2001.
(45) Berli, C. L. A.; Urteaga, R. Asymmetric capillary filling of non-Newtonian power law fluids. *Microfluid. Nanofluid.* **2014**, *17*, 1079−1084.
(46) Chalykh, A. E.; Stepanenko, V. Y.; Shcherbina, A.; Balashova, E. G. Adhesive Properties of Ethylene and Vinyl Acetate Copolymers. *Polym. Sci., Ser. D* **2009**, *2*, 8−15.
(47) Macosko, C. *Rheology: Principles, Measurements, and Applications*; Advances in interfacial engineering series; VCH: 1994.
(48) Kuwahara, R.; Tomita, R.; Ogawa, N.; Nakajima, K.; Takeda, T.; Uehara, H.; Yamanobe, T. Crystallization and hardening of poly(ethylene-co-vinyl acetate) mouthguards during routine use. *Sci. Rep.* **2017**, *7*, 7.
(49) Dion, M.; Larson, A. B.; Vogt, B. D. Impact of low-molecular mass components (oligomers) on the glass transition in thin films of poly(methyl methacrylate). *J. Polym. Sci., Part B: Polym. Phys.* **2010**, *48*, 2366−2370.
(50) Zhang, M.; Dobriyal, P.; Chen, J.-T.; Russell, T. P.; Olmo, J.; Merry, A. Wetting Transition in Cylindrical Alumina Nanopores with Polymer Melts. *Nano Lett.* **2006**, *6*, 1075−1079.
(51) Shin, K.; Woo, E.; Jeong, Y. G.; Kim, C.; Huh, J.; Kim, K.-W. Crystalline Structures, Melting, and Crystallization of Linear Polyethylene in Cylindrical Nanopores. *Macromolecules* **2007**, *40*, 6617−6623.
(52) Suzuki, Y.; Duran, H.; Steinhart, M.; Butt, H.-J.; Floudas, G. Homogeneous crystallization and local dynamics of poly(ethylene oxide) (PEO) confined to nanoporous alumina. *Soft Matter* **2013**, *9*, 2621−2628.
(53) Volynskii, A. L.; Yarysheva, A. Y.; Rukhlya, E. G.; Yarysheva, L. M.; Bakeev, N. F. Effect of Spatial Restrictions at the Nanometer Scale on Structuring in Glassy and Crystalline Polymers. *Polym. Sci., Ser. A* **2015**, *57*, 515−551.

DOI: 10.1021/acs.macromol.8b01504
Macromolecules 2018, 51, 8721−8728